Article

Coherent radio bursts from known M-dwarf planet-host YZ Ceti

J. Sebastian Pineda [1,4] ✉ **& Jackie Villadsen** [2,3,4]

Observing magnetic star–planet interactions (SPIs) offers promise for determining the magnetic fields of exoplanets. Models of sub-Alfvénic SPIs predict that terrestrial planets in close-in orbits around M dwarfs can induce detectable stellar radio emission, manifesting as bursts of strongly polarized coherent radiation observable at specific planet orbital positions. Here we present 2–4 GHz detections of coherent radio bursts on the slowly rotating M dwarf YZ Ceti, which hosts a compact system of terrestrial planets, the innermost of which orbits with a two-day period. Two coherent bursts occur at similar orbital phases of YZ Ceti b, suggestive of an enhanced probability of bursts near that orbital phase. We model the system's magnetospheric environment in the context of sub-Alfvénic SPIs and determine that YZ Ceti b can plausibly power the observed flux densities of the radio detections. However, we cannot rule out stellar magnetic activity without a well-characterized rate of non-planet-induced coherent radio bursts on slow rotators. YZ Ceti is therefore a candidate radio SPI system, with unique promise as a target for long-term monitoring.

The possible detection of coherent radio emissions associated with an exoplanetary system has motivated searches from megahertz to gigahertz frequencies because of the potential of such emissions to probe the unknown magnetic properties of exoplanets[1–3]. These proposed emissions are the consequence of a magnetic star–planet interaction (SPI) in which the dissipated energy powers electron cyclotron maser (ECM) emission, which occurs at the cyclotron frequency of the source region: megahertz-frequency radiation from the planet itself (fields of less than tens of gauss)[4,5], or megahertz to gigahertz radiation from the stellar corona (up to kilogauss fields) as the planetary perturbation is communicated starwards via Alfvén waves[6,7]. The latter mechanism, analogous to the Jupiter–Io flux tube interaction, relies on the host–satellite system being within a sub-Alfvénic regime, in which the Alfvén speed exceeds the stellar wind speed in the reference frame of the planet.

On the basis of the example of the Jupiter–Io system[8], we expect such sub-Alfvénic radio SPIs to appear as bursts of coherent emission with strong circular polarization lasting minutes to hours. While magnetic interaction can drive near-continuous radiation from the system, the angular beaming of the radio emission from the star–planet flux tube, as viewed by a distant observer, should cause the emission to appear as well-defined bursts dependent on the satellite orbital phase.

Recent results revealed 150 MHz ECM emission from M dwarf stars that could be consistent with sub-Alfvénic SPIs[9–11]. However, these systems need confirmation that a planetary satellite indeed drives the radio emission, with no planets yet found in campaigns targeting GJ 1151 (refs. 12,13). Polarized radio emission from Proxima Centauri (Prox Cen) exhibits possible orbital periodicity with Prox Cen b[14], but the planet's 11-day period places it at an orbital distance unlikely to have sub-Alfvénic interaction[15]. Moreover, the possibility of coherent radio bursts entirely of stellar origin remains important, as magnetically active M dwarf stars frequently exhibit polarized radio emissions[16,17], and the slowly rotating M dwarf Prox Cen exhibits stellar-flare-associated coherent radio bursts[18]. The radio flaring properties of inactive M dwarfs across megahertz to gigahertz frequencies are largely unknown, complicating efforts to exclude stellar activity as a cause of radio bursts. To disentangle stellar activity and SPIs, we aim to identify a system with coherent radio bursts and a very short-period

[1]Laboratory for Atmospheric and Space Physics, University of Colorado Boulder, Boulder, CO, USA. [2]Department of Physics and Astronomy, Bucknell University, Lewisburg, PA, USA. [3]Physics and Astronomy Department, Vassar College, Poughkeepsie, NY, USA. [4]These authors contributed equally: J. Sebastian Pineda, Jackie Villadsen. ✉e-mail: sebastian.pineda@lasp.colorado.edu
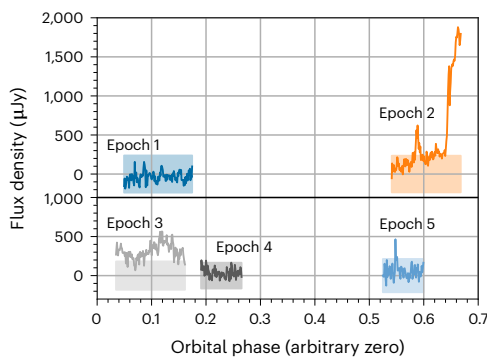
Fig. 1 | Time series of all 2–4 GHz observations of YZ Cet, phased using YZ Cet b's orbital period, binned to 3 min intervals. The first two epochs are shown on a separate panel to avoid overlap. The shaded regions show ±3 times the estimated error on the flux density for a 3 min time bin in each epoch, so that points above the shaded region have >3σ significance. The coherent burst in epoch 2 (phase -0.59) does not recur at the same orbital phase in epoch 5. The time error on phase-wrapping between epochs 1 and 5 is 5.3 min, negligible on the scale of this plot.

planet (less than a few days), which will enable long-term monitoring to test orbital periodicity—the clear evidence that could conclusively determine that any emissions are powered by SPI.

In this Article, we report the detection of 2–4 GHz coherent radio bursts from the known exoplanet host YZ Ceti (YZ Cet) using the National Science Foundation's Karl G. Jansky Very Large Array (VLA)[19]. This nearby slowly rotating star has three small planets orbiting in a compact configuration[20,21], including one in a two-day period. We discuss our radio observations in the context of SPIs, considering whether the YZ Cet planets could plausibly power the detected polarized bursts, and whether their recurrence suggests a solely stellar or possibly planet-induced origin.

Characterizing the radio bursts

We observed YZ Cet at 2–4 GHz with the VLA in 5 epochs: an initial programme of three daily 6.5 h observations from 30 November to 2 December 2019, and two 4 h follow-up observations on 2 February and 29 February 2020. Accounting for calibrator observations, our total on source time is ~26 h. Figure 1 shows the time series of all five epochs, phase-wrapped to the 2.02087 d orbital period of inner planet YZ Cet b[21], with an arbitrary zero phase because the radial velocity-determined orbital phase has an error of ~1/8 of the orbital period, too large to check whether bursts occur at quadrature. In the initial observations, the system was undetected (<36 μJy) in epoch 1, emitted multiple radio bursts in epoch 2 and produced slowly variable quiescent emission (313 ± 20 μJy) in epoch 3. In the follow-up observations, the star was undetected (<100 μJy) in epoch 4 and a single coherent burst occurred in epoch 5.

Figure 2 (left) shows the Stokes V dynamic spectrum of epoch 2 (see Methods for polarization time series). An hour-long coherent burst, with nearly 100% right circular polarization (RCP), occurs with peak flux density of 620 ± 80 μJy (in the Stokes I time series) around 2.3 h after the start of the observation. Three hours later, a bright flare occurs with weak polarization, which favours the incoherent gyrosynchrotron mechanism responsible for many solar and stellar flares[22]. The flare is preceded by enhanced Stokes I emission from 3 h to 5 h, with weak right polarization, which may be due to slowly varying quiescent emission (consistent with the variable quiescent emission in epoch 3) or pre-flare activity. An additional small burst, whose strong left circular polarization (LCP) favours a coherent mechanism, occurs during this epoch at 5.1 h, where it is superimposed on the incoherent flare. This LCP event may be due to accelerated electrons during the impulsive phase of a flare (for example, ref. 18). As this LCP feature is

probably associated with stochastic stellar flaring, we do not consider it further here. In our discussion, we focus on the RCP burst at 2.3 h, as we are searching for coherent bursts induced by SPIs.

We infer a coherent emission mechanism based on degree of polarization; for non-thermal processes, incoherent gyrosynchrotron emission with harmonic number $s \approx 10$–100 has less than 60% polarization for most viewing angles[23] whereas coherent emission often has up to 100% polarization. At gigahertz frequencies, without a measured source size, the brightness temperature indicates a non-thermal mechanism for both the strongly polarized bursts and weakly polarized flare and quiescent emission. For example, the 620 μJy peak flux density of the RCP burst at 3 GHz corresponds to a brightness temperature of $>1.5 \times 10^9$ K for an upper limit on source size of the full stellar disk; gigahertz-frequency coherent sources are probably much smaller, tracing to individual magnetic footpoints in the stellar corona. With the evidence available, we cannot differentiate between two possible coherent emission mechanisms, plasma emission and electron cyclotron maser, the latter of which is expected for SPIs. An ECM mechanism for the coherent bursts YZ Cet is plausible because many other M-dwarf radio bursts have been attributed to ECM due to high brightness temperature[9,10,24] or x-mode polarization[17]; however, we do not rely on the emission mechanism to assess an SPI origin. Instead, we search for evidence of orbital modulation of bursts to test the possibility that SPI drives the observed coherent bursts.

We scheduled the epoch 5 follow-up observations to encompass the same orbital phase as the RCP coherent burst in epoch 2. We detected a 1-min-long left-polarized coherent burst (Fig. 2, right) in these follow-up observations, with a peak flux density of 465 ± 70 μJy in the Stokes I time series with 3 min time bins (using 3 min for a consistent comparison with epoch 2). The orbital phase of the follow-up burst detection does not exactly match that of the observed epoch 2 bursts (Fig. 1), but instead occurs about 2 h earlier in the 2-day orbital period. Below, we consider whether the flux density and the relative timing of the bursts may be consistent with an SPI mechanism.

Assessing SPIs

The detection of multiple coherent radio bursts from YZ Cet prompts the question of whether the planets in the system could have powered the radio bursts. To answer this question, we must estimate the magnetized environment of YZ Ceti, and calculate the strength of the potential SPI.

For the environment, we adopted an isothermal stellar wind model for the YZ Cet system. The planets have orbital distances of 20 stellar radii or more[21] that are unlikely to be encompassed by closed stellar magnetic field lines, and thus the planets are probably intersecting open field lines that carry the stellar wind. We use two fiducial wind models (Methods). Model A assumes an open magnetic field entrained by a strong radial wind launched from the stellar surface, matching assumptions commonly used in approximate calculations in the literature (for example, refs. 7,9). Model B uses a weaker wind and a potential field source surface (PFSS) extrapolation to account for a closed field near the star. Incorporating a closed field region near the stellar surface, in particular, should provide a more realistic estimate of the radial field decay of any magnetized star. Uncertain model assumptions, regarding stellar mass-loss rate and magnetic field strength, can impact whether a planet orbits in the sub- or super-Alfvénic regime. Encouragingly, both of our fiducial models find that the innermost planets are within the sub-Alfvénic regime, allowing the planetary perturbation of the stellar magnetic field to communicate energy back towards the stellar surface to induce gigahertz emission. We expand on the effects of exploring the wind-model parameter space in Methods.

To compute the power available to drive planet-induced radio emissions, we used the frameworks of refs. 6,25. The latter (reconnection) computes the energy released through magnetic reconnection from the obstacle–field interaction, whereas the former (Alfvén wing)
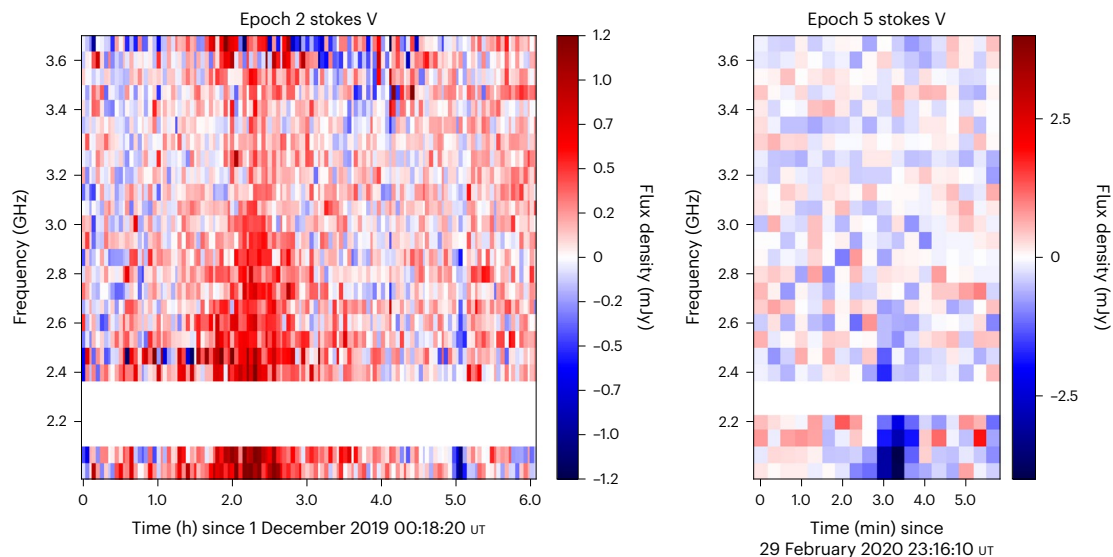
Fig. 2 | The 2–3.75 GHz Stokes V dynamic spectra of detected bursts.
Right-polarized bursts appear in red and left-polarized bursts in blue. Left: all
6.5 h of epoch 2, with an uncertainty of 19 μJy in each pixel of 3 min and 64 MHz.
Above ~3.4 GHz, the noise increases due to radio-frequency interference (RFI);
RFI flagging also causes the missing data (white region) around 2.3 GHz. Right:

a 6 min excerpt of epoch 5, with an uncertainty of 520 μJy in each pixel of 20 s
and 64 MHz. The events at 2.3 h and 5.1 h in epoch 2, and the epoch 5 event,
share a declining spectrum with the brightest emission observed near 2 GHz.
All three bursts have peak flux densities of >5σ in the dynamic spectrum.
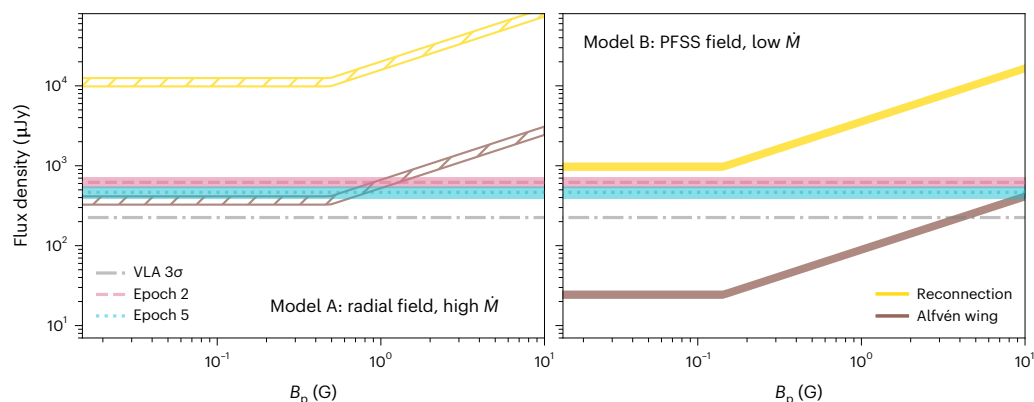

Fig. 3 | Predicted radio flux density due to SPI with YZ Cet b. Using our fiducial
wind models for the magnetized environment of the YZ Cet system, model A
(left) and model B (right), we predict radio flux densities generated by the planet
YZ Cet b, interacting with its host, according to the two interaction frameworks,
reconnection[25] (gold) and Alfvén wing[6] (brown). For a given planet dipole
magnetic field, the vertical extent of either SPI framework swath (reconnection

or Alfvén wing) corresponds to the flux density across the range of plausible
planet radii (Methods). The reconnection[25] predictions are stronger than those of
Alfvén wing[6]. Our measured flux densities of the brightest coherent radio bursts
from epoch 2 and epoch 5 are also shown (pink and blue) with shaded regions
corresponding to 1σ uncertainties. The horizontal grey dash-dot line shows the
typical 3σ RMS sensitivity in our VLA 3 min time series.

focuses specifically on the energy in Alfvén waves propagating back to
the host star from the same interaction. This computation depends on
all of the magnetic environment variables defined in our wind models A
and B, as well as on the magnetic properties of the planets, with stronger
planetary magnetic fields carving out a planetary magnetosphere that
serves as the enlarged obstacle radius for the SPI (Methods). Within
both frameworks, and using both models A and B for the magnetized
environments, we computed the possible strength of ECM radio bursts
associated with YZ Cet b, the closest-in planet and most likely to drive
appreciable radio emissions. We further varied the assumed planetary
dipole magnetic field strength, and the assumed planet radius to assess
their impact on the potential radio burst flux densities.

We demonstrate our results in Fig. 3, with model A on the left and
model B on the right, and different swathes for the reconnection and
Alfvén wing predictions in each panel. Under model A, the Alfvén wing
predictions neatly match the measured flux density of the bursts for a

weakly magnetized planet (~1 G); whereas the reconnection framework
strongly overpredicts the measured bursts. This marked difference is
probably due to model A overestimating stellar field strengths at the
location of the planet. Under the model B paradigm, in which PFSS
provides more realistic near-surface radial field decay, YZ Cet b could
power the emission with the reconnection framework, in the absence
of an intrinsic planetary magnetic field. However, according to the
Alfvén wing scenario, the planet would probably require a strong field
(≳a few gauss) to power the detected bursts.

There are many uncertain assumptions that go into these SPI flux
predictions, which in effect allow the prediction curves of Fig. 3 to
move up and down by several factors. Nevertheless, following our best
characterization of the system (model B), our calculations suggest that
if the reconnection framework is an accurate description of the phys-
ics, then the bursts could readily be produced by YZ Cet b through SPI.
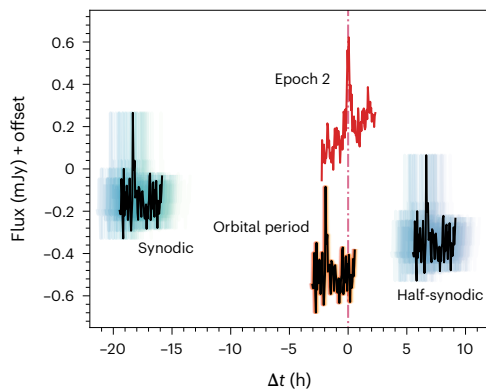Interestingly, if the Alfvén wing scenario is more applicable to these

Fig. 4 | Phase-wrapped time series of the portion of epoch 2 containing the RCP coherent burst, and all of epoch 5. By phasing the epoch 5 flux density light curves (black lines) at different periods (orbital period, synodic period and half-synodic period), compared with the epoch 2 burst (red, with vertical offset for clarity), we tested whether the radio burst occurrence is related to the orbit of YZ Cet b. The epoch 5 burst does not show a perfect recurrence at the orbital period ($\Delta t = 0$), but instead a difference in timing of ~2 h and ~6 h when using the half-synodic period. The burst phasing using the synodic period indicates a burst separation of almost a half-period; a full period is just over 48 h. The semi-transparent coloured lines (blue-green, purple and orange) below the epoch 5 curves illustrate the phase error due to uncertainty in the period measurements.

systems, then the radio detections would imply a substantial planetary magnetic field for the terrestrial planet.

After modelling the flux density of the detected radio bursts, we also considered their relative timing to evaluate their potential SPI nature. In Jupiter, the observed recurrence of the Io-induced radio emissions depends on both the orbital period P_{orb} and the rotation period P_{rot} of the tilted Jovian magnetic field (see within ref. 26). These define the synodic period ($P_{syn} = [P_{orb}^{-1} - P_{rot}^{-1}]^{-1}$) at which the satellite orbit returns to the same position relative to the host magnetic field. Reference [27] discussed the possible SPI periodicities in depth, noting the importance of the synodic period and half-synodic period, the latter defining a similar satellite position, but on the opposite side of the host magnetic field.

We phase-wrapped the time series of the RCP burst from epoch 2 and the time series of epoch 5, using three different relevant periods for YZ Cet b (Fig. 4): orbital (2.02087 d), synodic (2.08232 d) and half-synodic (1.04116 d). To calculate the synodic period, we used the photometric rotation period from ref. 21, 68.46 ± 1.00, leading to uncertainties of the order of an hour in the synodic and half-synodic phase-wrapping, whereas orbital period wrapping is precise to within a few minutes. When phase-wrapping with the orbital period, the epoch 5 burst takes place ~2 h before the phase of the epoch 2 polarized burst (phase difference, $\Delta\phi \approx 0.04$). Neither the synodic or half-synodic period phases the epoch 5 bursts closer to the time of the epoch 2 burst (Methods). These misalignments mean that our data cannot provide definitive evidence of SPI. We also applied a similar analysis to planets c and d, finding worse burst agreement in both time and phase. That there is near orbital recurrence for planet b, however, is tantalizing, as precise burst timing can depend on the complexities of magnetic geometry.

Changes in the near-surface magnetic field could impact the radio beaming angles and influence the observed timing of any planet-induced radio emissions—the importance of non-dipolar stellar field components increases closer to the star. The fact that the burst recurrence is closer in time to the half-synodic phasing than the synodic phasing also suggests that the epoch 5 burst occurs on the opposite side of the magnetic field to the epoch 2 burst, with the emission emerging from different poles. This point is consistent with

the change in polarity, RCP versus LCP, between the epoch 2 and epoch 5 bursts (Fig. 2). The difference in source origins with respect to the stellar magnetic field may also be responsible for the change in burst duration between epochs. If we assume the bursts are a consequence of the radio cone sweeping across the line of sight at a rate tied to the planet orbit, then the 1 h epoch 2 and 1 min epoch 5 durations would correspond to cone thicknesses of 7.4° and 0.12°, respectively. However, even when assuming intrinsically narrow (1°) cone widths, models of SPI radio dynamic spectra exhibit a wide range of burst durations depending on the extended source geometry, polarity and viewing angles[28]. A detailed map of the magnetic field structure (for example, from Zeeman–Doppler imaging (ZDI)) would enable confirmation of these behaviours and further apply consistency checks on the SPI scenario.

The polarized bursts may also be a consequence of ordinary stellar magnetic activity, such as flares, despite the star's slow rotation (~68 d). If we consider each of the polarized bursts to be independent stochastic events, we can consider our rate of detection as 2 events in 26 h (0.0769 h^{-1}) of radio monitoring (neglecting the small LCP events in epoch 2 as it may be flare substructure). Using simple Poisson statistics, the probability of seeing at least one event in the 3.6 h associated with epoch 5 is ~24%. By contrast, the probability of seeing one burst, on two separate occasions within 2 h of a given phase (a 4 h window) is only 5.1%—small but insufficient as conclusive evidence. It is thus plausible that the bursts could have no association with the planetary system and be a normal part of the radio stellar activity of slowly rotating M dwarfs, which is not yet well studied. The mechanisms powering the emission remain inconclusive, and we thus categorize YZ Cet as an SPI candidate, requiring further follow-up to discern the nature of the radio bursts.

Conclusions

We detected 3 GHz coherent radio bursts from the YZ Cet system, occurring in two of five observed epochs, where the coherent emission mechanism was indicated by a non-thermal brightness temperature and high degree of circular polarization. The 3 GHz frequency is consistent with ECM emission originating from the kilogauss fields expected at magnetic footpoints in the low stellar corona. The coherent radio bursts in two epochs nearly recurred in phase with the orbital period of YZ Cet b, after 90.9 d. The flux density of these bursts is roughly consistent with predictions for the average luminosity of sub-Alfvénic SPI[6,25], depending on the assumed conditions of the stellar environment and planetary magnetic field. On the basis of their luminosity and proximity in orbital phase, we consider these two events as candidate SPI events, but cannot rule out stellar magnetic activity as a possible cause. If SPI in this system is confirmed, the radio luminosity will enable estimation of the magnetic field strength of YZ Cet b, particularly when combined with refined measurements of the stellar magnetic field and the theory development of accurate flux density predictions.

The bursts do not recur at an exactly consistent orbital phase in follow-up observations (phase difference, $\Delta\phi \approx 0.04$), and show a greater degree of phase separation when considering the synodic and half-synodic periods, which take into account the rotation of the star. Recurrence with an orbitally dependent phase would provide a direct confirmation of planet-induced radio emission. In its absence, the possibility of orbital modulation remains: the preferred orbital phase for Io-induced bursts from Jupiter changes between two values over the course of Jupiter's rotational period (for example, ref. 26), due to the tilt of Jupiter's magnetic field. If the star's dipole field is tilted, then it rotated substantially between epochs 2 and 5, as their ~90 d separation is 1.3 times the star's ~68 d rotational period. In spite of this ambiguity, the result is suggestive: the orbital phase difference is small, and the periodicity may reflect an orbit-dependent window of visibility[6] for observing the beamed radio emission. Further observations that can test for orbital modulation include longer-term radio monitoring and

spectropolarimetric observations to determine the orientation of the star's large-scale magnetic field.

Monitoring to search for orbital modulation must contend with the 'foreground' of events caused by ordinary stellar activity. The slow rotation period of YZ Cet places it among stars with weak magnetic activity (for example, ref. 29). Slow rotators cannot power their luminous radio bursts by corotation breakdown in circumstellar plasma[9,30], a process responsible for some non-Io radio bursts from Jupiter. However, slowly rotating M dwarfs can still release energy through magnetic reconnection to produce luminous flares at other wavelengths such as ultraviolet (for example, ref. 31). The slow rotator Prox Cen has also produced coherent radio bursts near gigahertz frequencies[32], including an optical flare-associated event[18], suggesting that slowly rotating M dwarfs are capable of coherent bursts due to stellar activity. On the Sun, coherent bursts driven by magnetic reconnection are sometimes associated with incoherent gyrosynchrotron flares[23]; similarly, the coherent bursts and incoherent flare in epoch 2, occurring over the span of 4 h, may all derive from related processes in a magnetically active region.

A deeper understanding of polarized stellar radio bursts (rates, morphology, physical drivers) across megahertz to gigahertz frequencies would provide a notable advancement in disentangling such emissions from potential SPI signals. Searches for SPI emissions will need to contend with this foreground of stellar activity to be successful. In light of these considerations, and our own candidate detections, we propose a general criteria for assessing and confirming magnetic SPI at radio frequencies. The conditions are twofold: (1) recurrence of radio bursts at a period dependent on the orbit of a confirmed planet, and (2) a Poisson probability $p < 0.0027$ (equivalent to 3σ) of randomly observing those events within a narrow phase or time window, where that probability is based on an average burst rate determined by observing a wide range of orbital phases. If we again assume a stochastic rate of, $0.0769\ h^{-1}$, we would require 4 phased bursts within a 4 h phase window to exceed this probability threshold; at 5σ confidence, we would require 10 such bursts. It is prior knowledge of the planet's period to high precision that can enable high confidence in the SPI interpretation given a low probability of randomly recurring stochastic events. Radio non-detections, spanning a broad phase range, are important for an accurate measurement of a stochastic radio burst rate to distinguish the phases of SPI enhancement from standard stellar processes. These criteria rely largely on multi-epoch radio monitoring, and can be corroborated by complementary observations of the stellar magnetic field and planetary geometry. For such long-term monitoring to test periodicity, the confirmed planet of YZ Cet in a 2 d period makes it a uniquely promising case study for magnetic SPIs.

Methods

Stellar characterization

Table 1 details the physical stellar properties for our target YZ Cet and comparison objects Prox Cen and GJ 1151, determined by combining multiple empirical relations to jointly constrain the mass, radius and bolometric luminosity (method in ref. 33). The estimates employ a precise parallax from Gaia Data Release 2 (ref. 34), with the effective temperature derived from combining the luminosity and radius. The bolometric flux measurements for YZ Cet and GJ 1151 are from ref. 35, and for Prox Cen they are from ref. 36. We further quote additional relevant activity properties, including the stellar rotation period (68.46 ± 1.00), from their respective references. There is a more precise V-band rotation period of 68.4 ± 0.05 measured[21], but the formal statistical error may not encompass all forms of systematic error. To explore the impact of rotation period uncertainty over the ~90 d separation between epochs 2 and 5, we opted to use the less precise period when phase-wrapping with the synodic periods, finding that it broadens the uncertainty curves but does not impact our conclusions. We also note that optical flaring can be seen in each object's Transiting Exoplanet Survey Satellite[37] light curves.

Table 1 | Slowly rotating M dwarfs with coherent radio detections

Property	YZ Ceti	Proxima Centauri	GJ 1151
Spectral type	M4.5 (ref. 57)	M5.5 (ref. 58)	M4.5 (ref. 57)
Distance (pc)	3.712	1.301	8.038
Mass ($M_\odot$)	0.137±0.003	0.123±0.003	0.168±0.004
Radius ($R_\odot$)	0.163±0.007	0.147±0.005	0.192±0.008
L_{bol} (10^{30} erg s^{-1})	8.6±0.1	6.00±0.08	13.0±0.2
T_{eff} (K)	3,110±70	2,990±50	$3,181\pm^{65}_{63}$
$\log_{10}[L_X/L_{bol}]$	−4.13 (ref. 43)	−4.4 (ref. 59)	<−4.19 (ref. 43)
$\log_{10}[L_{H\alpha}/L_{bol}]$	−4.32 (ref. 60)	−4.20 (ref. 58)	−4.75 (ref. 60)
P_{rot} (d)	~68.5 (ref. 21)	~89 (ref. 61)	~130 (ref. 62)
Bf (kG)	~2.2 (ref. 46)	~0.6 (ref. 63)	—
Planetary system	Y	Y	?[12,13]
Planet periods (d)	2.02, 3.06, 4.66 (ref. 21)	5.1243 [a] (ref. 64), 11.186 (ref. 65)	—
Planetary a/R_s	21.6, 28.4, 37.6 (ref. 21)	42.2[a] (ref. 64), 70.95 (ref. 65)	—
Planetary $m_p\sin i$ ($M_\oplus$)	0.70, 1.14, 1.09 (ref. 21)	0.40[a] (ref. 64), 1.27 (ref. 65)	—
Frequency (GHz)	3.0	0.9–2.0	0.145
$L_{v,iso}$[b] (10^{12} erg s^{-1} Hz^{-1})	10	6–100 (refs. 14,18,32)	100 (ref. 9)
Burst duration (h)	1	0.07–38.4+	>8
Polarization (%)	~93	~90–100	~64

[a]The quoted innermost planet for Prox Cen is a new candidate from ref. 64. [b]$L_{v,iso} = 4\pi d^2 S_v$ assumes isotropic radiation, where S_v is the approximate peak flux density of an event in this work (YZ Cet) or cited works. This assumption is not accurate for coherent emission, but it provides a distance-independent measure for comparing stars without relying on uncertain estimates of the true beaming angle. Symbols used above: L_{bol}: Bolometric luminosity. T_{eff}: Effective temperature. L_x: X-ray luminosity. $L_{H\alpha}$: H-alpha luminosity. Bf: Average surface magnetic field from Zeeman broadening. m_p: Planetary mass. i: Planetary orbital inclination. $L_{v,iso}$: Radio luminosity. v: frequency. d: stellar distance from Earth.

Radio data analysis

For our VLA observations of YZ Cet we used 3C147 as flux calibrator and J0116−2052 as gain calibrator, and calibrated the data in CASA[38] using the VLA pipeline. The VLA was in compact configuration: D in epochs 1–3, DnC in epoch 4 and C in epoch 5. We observed with the phase centre located halfway between YZ Cet and the 150 mJy nearby source PMN J0112−1658 (7.5 arcmin away from YZ Cet), to keep that source within the main lobe of the primary beam, then shifted the phase centre to the location of the star before imaging. We imaged the first three epochs together and each of the two follow-up epochs separately, using CASA's 'tclean' task with W projection, multiscale imaging and multifrequency synthesis with three Taylor terms. We used natural weighting to maximize point source sensitivity.

For each dataset, we performed self-calibration on the target field using CASA's 'gaincal' command: one or two rounds of phase-only self-calibration, followed by one or two rounds of amplitude and phase self-calibration. For amplitude self-calibration, we used gaincal's solnorm=true parameter, normalizing gain amplitudes to an average value of one to avoid artificially increasing flux density. For example, in the self-calibrated image of epochs 1–3 (Supplementary Fig. 1), the peak flux density of PMN J0112−1658 remained consistent (148.4 mJy before self-calibration, 148.5 mJy after), while the uncertainty substantially improved: the root-mean-square error in a region near YZ Cet that is empty of bright sources was 120 μJy before, and 25 μJy after self-calibration.

After imaging, we masked the star out of the model so that the model contained only background sources, then subtracted the model

from the visibility data to obtain residual visibilities containing only the star and noise. Supplementary Figs. 2 and 3 show images of radio bursts in epochs 2 and 5 in the background-subtracted data. In Stokes I, residual sidelobes are visible due to imperfect subtraction of PMN J0112−1658.

With the star at the phase centre, we used the 'plotms' task to average the residual visibilities across all baselines and frequencies, yielding a complex-valued time series. The real component is equivalent to the centre pixel of a natural-weighted image, yielding the flux density of the star. The imaginary component should not contain stellar flux, but exhibits comparable levels of noise due to thermal noise, radio-frequency interference (RFI), and sidelobes of imperfectly subtracted background sources. These residual background sidelobes can cause 'ripples' in the time series as the sidelobe pattern evolves over time. We calculated the standard deviation of the imaginary component to estimate the effective noise levels in the time series including these factors. We used the imaginary component of the time series to estimate noise levels because, in epochs without clearly detected stellar variability, the real and imaginary components have roughly similar standard deviations. For example, in epoch 1, the Stokes I standard deviation is 69 μJy (real) and 79 μJy (imaginary), and the Stokes V standard deviation is 50.5 μJy (both real and imaginary). The greater standard deviation for Stokes I than Stokes V illustrates the effect of residual sidelobes of background sources.

For 3 min integrations, we measured noise levels of 55–80 μJy in the Stokes I time series and 37–50 μJy in Stokes V. Without source confusion, the VLA's theoretical sensitivity in 3 min is 22 μJy. As source confusion is not an issue in Stokes V, the elevated Stokes V noise levels are probably due to RFI, with data loss due to RFI flagging and low-level RFI in the remaining data. The Stokes I noise levels are affected by both RFI and imperfect background-source subtraction; both of these effects are enhanced by the VLA's compact configuration.

Figure 1 shows the resulting time series as a function of orbital phase, where the shaded region shows ±3 times the estimated noise level on flux density in each of the 3 min time bins in that epoch. Supplementary Figs. 4 and 5 show detailed time series of epochs 2 and 5, the two epochs with coherent bursts. To identify bursts, we required a flux increase of >3σ during the burst compared with before or after the burst. For example, in epoch 2 (Supplementary Fig. 4), the events at 2.3 h, 5.1 h and 5–6 h satisfy this criterion, whereas a possible left-polarized event at 3.1 h constitutes only a 2σ flux enhancement.

For epochs without bursts, we measured or placed an upper limit on the quiescent emission levels using an image of the full epoch duration after background-source subtraction. For epoch 1, we measured an intensity of $I = -39$ μJy per beam in the image at the star's location (star undetected) and an RMS in the image near the star's location of $\sigma = 25$ μJy per beam, leading to a 3σ upper limit on source flux density of: $S < 3\sigma = 75$ μJy. In epoch 3, the star was detected with a peak flux density of 313 ± 20 μJy (Stokes I) and 18.7 ± 5.3 μJy (Stokes V). In epoch 4, the star was undetected with an intensity of 36 ± 21 μJy at its location in the image, yielding a 3σ upper limit of 64 μJy on flux density. Weakly polarized, non-thermal, slowly varying quiescent emission on M dwarfs, such as in epoch 3, is typically attributed to incoherent gyrosynchrotron emission[39].

The degree of circular polarization of a signal is $r_c = V/I = (RR - LL)/(RR + LL)$, where RR and LL are the right circular polarization and left circular polarization visibility data, respectively. To assess the bursts' degree of circular polarization, we used a maximum likelihood approach to estimate r_c and construct a 68% confidence interval. To calculate the likelihood, we assumed RR and LL are Gaussian distributed, obtaining the standard deviation for each from the imaginary component of the time series. We generated a probability distribution function (PDF) for obtaining the data in terms of model parameters S_I (Stokes I flux density) and r_c, then marginalized the distribution across S_I to obtain a PDF for r_c alone. The black line in Supplementary

Figs. 4 and 5 shows the value of r_c at which the PDF peaks, and the grey confidence interval shows the range of r_c that lies from 0.16 to 0.84 in the cumulative distribution function.

We produced dynamic spectra (Fig. 2 and Supplementary Fig. 6) for all of epoch 2 and for a short time period surrounding the epoch 5 burst, using the baseline-averaging code described in ref. 17. The flux density uncertainties quoted in the caption are calculated using the imaginary component of the dynamic spectrum (which does not contain stellar emission), by taking the standard deviation in each frequency channel then calculating the median across all channels. The peak flux densities in Stokes V for the epoch 2 bursts at 2.3 h and 5.1 h both exceed 5σ, as does the epoch 5 burst. The incoherent flare in epoch 2 has weak right polarization, appearing only faintly in Stokes V except for the coincident LCP burst at 5.1 h, and in Stokes I it spans the entire 2–3.7 GHz band, consistent with the broadband nature of gyrosynchrotron emission.

In epoch 2, the right-polarized burst and the left-polarized burst at 5.1 h both are brightest at lowest frequencies (<3 GHz). Like the two clearest features in the epoch 2 dynamic spectrum, the epoch 5 event is also brightest at the lowest frequencies. These three events that appear clearly in the dynamic spectra drop off above 2.5–3 GHz. If the emission process is the cyclotron maser, this indicates that the maximum magnetic field in the source regions is of the order of 1 kG.

Stellar magnetospheric environment

To determine whether SPIs could have powered our observed polarized radio emissions we needed to characterize the likely magnetospheric environment impacting the YZ Cet planetary system. We considered two models: (1) a magnetosphere defined by a radial isothermal stellar wind whose properties are set by the corona and the surface magnetic field strength, and (2) a PFSS extrapolation of typical M-dwarf ZDI measurements including an isothermal stellar wind solution beyond the source surface[40]. As the magnetic field and wind environments of low-mass stars are very uncertain, this approach explores the effects of a range of likely stellar magnetic field strengths experienced by the YZ Cet planets.

The first approach, often employed in the literature, uses a stellar wind originating from the stellar surface, which overestimates the magnetic field at the planet location because it does not take into account the rapid radial decay of closed field lines near the stellar surface (for example, ref. 7). The second approach accounts for this effect by using a more realistic stellar magnetic field topology (for example, ref. 40); however, the inherent assumptions exclude additional stresses to the magnetic field, and may underestimate the strength of the magnetic field at planetary distances from the star, beyond a poorly constrained source surface.

Model A (radial stellar field, high $\dot{M}$). To formulate the radial stellar wind solution we used a Weber wind model[41], which solves the ideal magnetohydrodynamics problem in spherical coordinates for an axisymmetric equatorial wind propelled by a rotating star. Note that there is a typo in their equation (23). In the last term of the denominator in brackets, the factor $\Omega^2 r^2 M_A^2$ should be $\Omega^2 r^2 M_A^4$, for angular rotation rate Ω, radial coordinate r, and radial Alfvénic Mach number M_A. Their solution is similar to that of ref. 42, but self-consistently incorporates the stresses of the ionized wind on the magnetic field anchored to the rotating star. We depart from ref. 41, by employing an isothermal wind, a subcase of their general polytropic approach. The physical wind solution is the one that smoothly passes through the three critical points (one sonic, two magnetic)[41], constraining the solution and fixing the initial radial wind velocity for our choice of boundary conditions. The coupled solution requires as inputs: stellar mass, radius and rotation rate (Table 1), as well as coronal plasma temperature, an average mass-loss rate and the radial magnetic field strength at the surface (see below). With these assumptions, we numerically solved for the wind

radial profile. In practice, the system of equations incorporating the critical points fixes the total energy, a constant of the motion. We then employed the energy equation to numerically solve for the radial speed as a function of distance from the star. The other system properties could then be determined from the radial wind profile[41]. In summary, the important variable parameters for the boundary conditions reduce to the coronal temperature, radial magnetic field strength and mass-loss rate.

For this model (A), we assumed a coronal temperature of $k_B T = 0.25$ keV $\approx 3 \times 10^6$ K, a constant mass-loss rate of $\dot{M} \equiv 4\pi\rho u r^2 = 10^{-13} M_\odot$ yr^{-1} = 5 $\dot{M}_\odot$ (fives times the mass-loss rate of the Sun), and radial field of B_r = 220 G. The assumed constant mass-loss rate sets the relationship between the mass density profile, ρ, and the radial wind speed, u. The coronal temperature is similar to that of other inactive late M dwarfs, based on their X-ray observations (for example, refs. 43,44). The mass-loss rate is a compromise between the expected rates for similar stars based on their Rossby numbers (0.5 for YZ Cet)[40], and the low rate of Prox Cen (see within ref. 15), which has similar physical properties, albeit with a weaker magnetic field strength (Table 1).

For the estimate of the average radial surface magnetic field strength of YZ Cet, we utilized the measured large-scale field topology of Prox Cen, from ref. 45, as no such measurements of YZ Cet are yet available. Because of their similar properties (Table 1), Prox Cen is a useful analogue for interpreting the magnetic properties of YZ Cet, and is one of the few slowly rotating late M dwarfs with a measured field topology from ZDI. We scaled the measured magnetic field of Prox Cen, in its spherical harmonic decomposition, based on the measured Zeeman broadening measurement of YZ Cet, $<B_{ZB}>$ = 2,200 G (ref. 46). We defined the scaling to achieve an average field flux strength ratio of $\zeta \equiv <B_{ZDI}>/<B_{ZB}> \approx 0.1$, and thus an average radial surface field of 220 G. We chose ζ = 0.1 as a representative value for the sample of stars with similar properties in ref. 47 that have both kinds of Zeeman measurements. The low value of ζ originates from field cancellation in the Stokes V ZDI measurements, as opposed to the Stokes I ZB measurements that include the total field strength. It is worth noting that the YZ Cet Zeeman broadening measurement is a high outlier for its Rossby number of ~0.5 (ref. 48), and the source measurements[46] may be systematically high[48], especially for slow rotators. However, ZDI has measured M-dwarf ζ values up to ~0.3 (Prox Cen[45]), so our estimated average large-scale field of 220 G may be reasonable even if the current YZ Cet ZB measurement is an overestimate. With an average large-scale field of 220 G, surface variations and small-scale fields in the low stellar corona could still lead to regions with kilogauss field strengths, plausibly allowing ECM emission at 2–3 GHz.

Model B (PFSS stellar field, low $\dot{M}$). For model B, we used the same assumptions for the wind properties with two key differences. The first is that we moved the inner boundary of the Weber wind model, where the stellar field is purely radial, to 4.5 stellar radii, consistent with magnetohydrodynamic simulations of M-dwarf winds (Table 2 in ref. 49). Shifting this 'source surface' outwards accounts for closed magnetic field lines near the surface. We modelled this closed field by filling the space between the stellar surface and the wind source surface with a PFSS extrapolation (for example, ref. 50) based on the field topology of Prox Cen, scaled to yield an average large-scale radial field of 220 G at the stellar surface. The PFSS extrapolation thus sets the average radial magnetic field strength at 4.5 stellar radii from the star. Second, we also assumed a 20-times lower mass-loss rate of 0.25 $\dot{M}_\odot$, comparable to the upper limit on Prox Cen wind from ref. 51 and consistent with the predicted rate from ref. 15. This value is also close to the expectation (~0.23 $\dot{M}_\odot$) calculated from the relation between X-ray surface flux and mass-loss rate[52,53]. We compare these distinct magnetic environments in Supplementary Fig. 7.

We further illustrate some properties of model B in Supplementary Fig. 8, showing the velocities relevant to the wind (top panel), and

the total wind pressure throughout the model environment around YZ Cet. We considered model B to correspond to our most realistic estimate of the average magnetized environment pervading this planetary system, whereas model A encapsulates typical assumptions in the literature treatment of these questions. While informed by the literature, the wind parameters are typically uncertain for low-mass stars, but as we employed an analytic model, we can readily change the input assumptions to determine their effect on the potential for the YZ Cet planetary system to power radio emissions (see below). To provide some intuition for the isothermal wind solution and the impacts of these parameter assumptions, we note that changing the temperature is the most impactful parameter determining the wind velocity, changes in the mass-loss rate largely impact the wind density, and the radial field strength scales the overall magnetic field as the azimuthal field component is much weaker for slowly rotating systems. In the absence of a three-dimensional wind simulation (for example, ref. 15), these simplified isothermal approaches provide a reasonable means to examine the approximate interplanetary environment conditions[53].

Planet-induced radio emission

Our detection of polarized radio bursts from YZ Cet prompts the question of whether the coherent radio emission could have been powered by the magnetic interaction of the star with its planets (see within ref. 1). We used models A and B (described above), to define the magnetized stellar wind filling the environment of the YZ Cet planetary system. When this wind interacts with the planets, the dissipated energy can power auroral radio emissions. We estimated the available power through this interaction using the frameworks of ref. 25 (reconnection) and ref. 6 (Alfvén wings), similar to the approach taken by ref. 9.

The available power released by magnetic reconnection[25] is

$$S_l = \frac{1}{4}\gamma R_o^2 v B^2, \qquad (1)$$

in cgs units, where γ is a geometric factor, R_o is the radius of the obstacle, that is, the planetary magnetosphere, v is the velocity of interaction in the frame of the planet, and B is the star's magnetic field strength at the planet location. Similarly, the available power transmitted through Alfvén wings[6], a prediction valid in the low Mach number regime, is

$$S_s = \frac{1}{2}\bar{\alpha}^2 R_o^2 v^2 B \sin^2\theta \sqrt{4\pi\rho}, \qquad (2)$$

as expressed by ref. 3, where $\bar{\alpha}$ is an interaction strength, θ indicates the angle between the wind's relative velocity vector and the magnetic field in the planet's frame of reference, and ρ is the mass density of the magnetized flow. These two approaches differ by a factor of twice the Alfvénic Mach number[6] and a geometric factor. We take the wind properties for models A and B, and use these expressions to estimate the expected power available to generate ECM radio emissions. At the planet's location, the wind and magnetic field are aligned and nearly radial due to the star's slow rotation, but the planet's orbital velocity (small relative to wind speed) gives θ a small, non-zero value. We focused on YZ Cet b as the closest-in planet and most likely to power the detected hundreds of microjansky bursts in our radio datasets.

In evaluating equations (1) and (2), we take the middle value of the geometric factor, so $\gamma \to 1/2$, and consider the interaction strength $\bar{\alpha} \to 1$. The former is justified by our ignorance of the exact geometry of the interacting magnetic fields[25]. For the latter, we justify the assumption of the interaction strength based on the likely conductivity of the planetary obstacle through its magnetosphere or ionosphere, considering the environments of the large close-in rocky planets of the YZ Cet system to have high Pederson conductivities (see Appendix A of ref. 7).

The last remaining variable in the power expressions is the planetary obstacle radius, R_o. This is defined by the size of the planetary

magnetosphere, or at a minimum the radius of the planet itself assuming a thin ionosphere. We use the pressure balance between the supposed planetary field and the wind to define the radius of the planetary magnetopause:

$$R_o = R_p \left(\frac{B_p^2}{8\pi\rho v^2 + 8\pi\rho kT/\mu m_p + B^2} \right)^{1/6},$$ (3)

where B_p is the assumed planetary dipole field strength, $\mu = 0.5$ for a fully ionized hydrogen wind and m_p is the proton mass. If the ratio of R_o/R_p from equation (3) falls below unity, we instead use R_p as the obstacle radius.

The YZ Cet system was characterized with radial velocity measurements and does not exhibit transits, so the planet radii are unknown. The planets are likely to be roughly Earth-sized, and YZ Cet b has a minimum mass of $0.7\,M_\oplus$. For the radii of YZ Cet b we consider a range from $R_p = 0.89\,R_\oplus$ to $R_p = 1\,R_\oplus$, where the lower bound corresponds to the radius of the minimum mass assuming it also has an Earth-like density. As the planet is roughly Earth-sized, we explore a range of planetary dipole field strengths starting from 1 G (Earth-like), increasing it by an order of magnitude (10 G), and decreasing it to below the stellar field strength at the planet location (effectively unmagnetized). These values set the abscissa range in Fig. 3.

With these assumptions, we can compute the energy available to power auroral radio bursts from YZ Cet, using both the reconnection and Alfvén wing prescriptions, as well as considering both the model A and model B wind environments. To convert the power to a possible burst radio flux density we use

$$F_\nu = \frac{\epsilon S}{\Omega \Delta \nu d^2},$$ (4)

where S comes from equation (1) or equation (2), $\epsilon = 0.01$ is the radio efficiency factor[1,6], $\Delta\nu = 3$ GHz is the emission bandwidth, for which we assume the emission spans from low frequencies to our emission band, $d = 3.712$ pc is the distance to the star, and we use $\Omega = 0.16$ sr for the beaming angle based on the observed value for Jupiter–Io radio emission[54]. The results of our calculations are shown in Fig. 3, and discussed in the main text.

SPI parameter space

The predicted flux densities for SPI depend on a variety of unknown properties for the magnetized environment, most prominently the assumed stellar mass-loss rate, and the stellar field strength. Above, we chose models A and B to represent a range of values consistent with the literature and the known physical properties of the star. Below, we explore two specific effects related to these assumptions: the range of mass-loss rates consistent with the SPI scenario and the dependence of the SPI power on the assumed stellar magnetic field.

Constraints on mass-loss rate. If our detected bursts are indeed powered by sub-Alfvénic SPI, then the corresponding planet must be within the Alfvén surface of the stellar environment. Using our isothermal wind solution, we explored the impact of the assumed mass-loss rate on the Alfvénic Mach number at the position of the planets around YZ Cet. We show these results in Supplementary Fig. 9. Both fiducial models A and B allow for an increase of an order of magnitude in the assumed mass-loss rate before any planets go beyond the Alfvén surface, and even more before YZ Cet b becomes super-Alfvénic.

Because the star is rotating slowly, the wind speed and stellar field are largely radial, and as the orbital motion of the planets is small compared with the wind speed, the results in Supplementary Fig. 9 are well approximated by

$$\frac{v}{v_A} \approx \frac{\sqrt{\dot{M} v_r}}{B_r},$$ (5)

where the velocity and field on the right-hand side correspond to the radial components evaluated at the position of the planets. For our fiducial model A ($5\,\dot{M}_\odot$), the planets a, b and c, become super-Alfvénic at mass-loss rates of approximately 150, 80 and 50 times $\dot{M}_\odot$, respectively. For our fiducial model B ($0.25\,\dot{M}_\odot$), the planets a, b and c, become super-Alfvénic at mass-loss rates of approximately 13.5, 7.5 and 4 times $\dot{M}_\odot$, respectively. Increasing the assumed stellar magnetic field would increase the distance corresponding to the Alfvén surface, and increase the planets' corresponding sub/super-Alfvénic transition mass-loss rate. If our radio detections are powered by the interaction of YZ Cet b with its host, it should imply that YZ Cet has a mass-loss rate within these bounds, probably $<13.5\,\dot{M}_\odot$, using our more realistic model B stellar field topology.

Scaling the stellar magnetic field. As discussed when introducing models A and B above, we conservatively assumed a surface radial average field strength of 220 G, but this may be an underestimate. For both our models A and B, scaling the magnetic field at the surface towards higher values linearly scales the field at the location of the planet, and similarly scales the minimum predicted SPI flux density as a function of planet field strength (flat regions in Fig. 3). The turning points in Fig. 3 also shift towards higher planet field strengths, as their position encodes where the stellar and planetary fields balance.

For model A, a stellar field increase of a factor of 2 or 3 places flux density predictions above the measured bursts, for both the reconnection and Alfvén wing mechanisms. If our radio detections are indeed SPIs, this underscores that model A overestimates the stellar field strength at the planet's location by not accounting for closed field structures. Literature SPI predictions with stellar radial fields, like what we have assumed with model A, may overpredict both SPI intensities and the size of the Alfvén surface and which planets it encompasses.

For model B, an increase in the field strength of a factor of 2 or 3 pushes both the reconnection and Alfvén wing predictions to higher values. While the reconnection prediction would become more discrepant with the measured burst flux densities, it would place the Alfvén wing prediction consistent with smaller (but non-negligible) planetary dipole fields. If our detections are indeed SPIs, and if additional measurements reveal that the average global field of YZ Cet substantially exceeds 220 G, then our result would support model B (accounting for closed field near the surface) over model A (open stellar field), and the Alfvén wing mechanism over the reconnection mechanism.

Data availability
The radio data used in this publication are available through the NRAO archive (data.nrao.edu) under project code VLA/19B-222.

Code availability
The raw radio data were processed with publicly available software package CASA[38] and NRAO's VLA calibration pipeline. The codes describing the model stellar wind implementation are available upon reasonable request to the corresponding author. The public Python packages that are part of astropy also aided in the analysis and presentation of results[55,56].

References
1. Zarka, P. Plasma interactions of exoplanets with their parent star and associated radio emissions. *Planet. Space Sci.* **55**, 598–617 (2007).
2. Hallinan, G. et al. Looking for a pulse: a search for rotationally modulated radio emission from the hot Jupiter, τ Boötis b. *Astrophys. J.* **762**, 34 (2013).

3. Pineda, J. S. & Hallinan, G. A deep radio limit for the TRAPPIST-1 system. *Astrophys. J.* **866**, 155 (2018).

4. Lazio, W. et al. The radiometric Bode's law and extrasolar planets. *Astrophys. J.* **612**, 511 (2004).

5. Grießmeier, J. M., Zarka, P. & Spreeuw, H. Predicting low-frequency radio fluxes of known extrasolar planets. *Astron. Astrophys.* **475**, 359–368 (2007).

6. Saur, J., Grambusch, T., Duling, S., Neubauer, F. M. & Simon, S. Magnetic energy fluxes in sub-Alfvénic planet star and moon planet interactions. *Astron. Astrophys.* **552**, A119 (2013).

7. Turnpenney, S., Nichols, J. D., Wynn, G. A. & Burleigh, M. R. Exoplanet-induced radio emission from M dwarfs. *Astrophys. J.* **854**, 72 (2018).

8. Queinnec, J. & Zarka, P. Io-controlled decameter arcs and Io–Jupiter interaction. *J. Geophys. Res.* **103**, 26649–26666 (1998).

9. Vedantham, H. K. et al. Coherent radio emission from a quiescent red dwarf indicative of star–planet interaction. *Nat. Astron.* **4**, 577–583 (2020).

10. Callingham, J. R. et al. The population of M dwarfs observed at low radio frequencies. *Nat. Astron.* **5**, 1233–1239 (2021).

11. Pope, B. J. S. et al. The TESS view of LOFAR radio-emitting stars. *Astrophys. J. Lett.* **919**, L10 (2021).

12. Pope, B. J. S. et al. No massive companion to the coherent radio-emitting M dwarf GJ 1151. *Astrophys. J. Lett.* **890**, L19 (2020).

13. Perger, M. et al. The CARMENES search for exoplanets around M dwarfs. No evidence for a super-Earth in a 2-day orbit around GJ 1151. *Astron. Astrophys.* **649**, L12 (2021).

14. Pérez-Torres, M. et al. Monitoring the radio emission of Proxima Centauri. *Astron. Astrophys.* **645**, A77 (2021).

15. Kavanagh, R. D. et al. Planet-induced radio emission from the coronae of M dwarfs: the case of Prox Cen and AU Mic. *Mon. Not. R. Astron. Soc.* **504**, 1511–1518 (2021).

16. Lynch, C. R., Lenc, E., Kaplan, D. L., Murphy, T. & Anderson, G. E. 154 MHz detection of faint, polarized flares from UV Ceti. *Astrophys. J. Lett.* **836**, L30 (2017).

17. Villadsen, J. & Hallinan, G. Ultra-wideband detection of 22 coherent radio bursts on M dwarfs. *Astrophys. J.* **871**, 214 (2019).

18. Zic, A. et al. A flare-type IV burst event from Proxima Centauri and implications for space weather. *Astrophys. J.* **905**, 23 (2020).

19. Perley, R. A., Chandler, C. J., Butler, B. J. & Wrobel, J. M. The Expanded Very Large Array: a new telescope for new science. *Astrophys. J. Lett.* **739**, L1 (2011).

20. Astudillo-Defru, N. et al. The HARPS search for southern extra-solar planets. XLII. A system of Earth-mass planets around the nearby M dwarf YZ Ceti. *Astron. Astrophys.* **605**, L11 (2017).

21. Stock, S. et al. The CARMENES search for exoplanets around M dwarfs. Characterization of the nearby ultra-compact multiplanetary system YZ Ceti. *Astron. Astrophys.* **636**, A119 (2020).

22. Güdel, M. Stellar radio astronomy: probing stellar atmospheres from protostars to giants. *Annu. Rev. Astron. Astrophys.* **40**, 217–261 (2002).

23. Dulk, G. A. Radio emission from the Sun and stars. *Annu. Rev. Astron. Astrophys.* **23**, 169–224 (1985).

24. Osten, R. A. & Bastian, T. S. Ultrahigh time resolution observations of radio bursts on AD Leonis. *Astrophys. J.* **674**, 1078–1085 (2008).

25. Lanza, A. F. Stellar coronal magnetic fields and star–planet interaction. *Astron. Astrophys.* **505**, 339–350 (2009).

26. Zarka, P. et al. Jupiter radio emission induced by Ganymede and consequences for the radio detection of exoplanets. *Astron. Astrophys.* **618**, A84 (2018).

27. Fischer, C. & Saur, J. Time-variable electromagnetic star–planet interaction: the TRAPPIST-1 system as an exemplary case. *Astrophys. J.* **872**, 113 (2019).

28. Hess, S. L. G. & Zarka, P. Modeling the radio signature of the orbital parameters, rotation, and magnetic field of exoplanets. *Astron. Astrophys.* **531**, A29 (2011).

29. Newton, E. R. et al. The Hα emission of nearby M Dwarfs and its relation to stellar rotation. *Astrophys. J.* **834**, 85 (2017).

30. Nichols, J. D. et al. Origin of electron cyclotron maser induced radio emissions at ultracool dwarfs: magnetosphere–ionosphere coupling currents. *Astrophys. J.* **760**, 59 (2012).

31. Loyd, R. O. P. et al. The MUSCLES Treasury Survey. V. FUV flares on active and inactive M dwarfs. *Astrophys. J.* **867**, 71 (2018).

32. Slee, O. B., Willes, A. J. & Robinson, R. D. Long-duration coherent radio emission from the dMe star Proxima Centauri. *Publ. Astron. Soc. Aust.* **20**, 257–262 (2003).

33. Pineda, J. S., Youngblood, A. & France, K. The M-dwarf ultraviolet spectroscopic sample. I. Determining stellar parameters for field stars. *Astrophys. J.* **918**, 40 (2021).

34. Gaia Collaboration Gaia Data Release 2. Summary of the contents and survey properties. *Astron. Astrophys.* **616**, A1 (2018).

35. Mann, A. W., Feiden, G. A., Gaidos, E., Boyajian, T. & von Braun, K. How to constrain your M dwarf: measuring effective temperature, bolometric luminosity, mass, and radius. *Astrophys. J.* **804**, 64 (2015).

36. Boyajian, T. S. et al. Stellar diameters and temperatures. II. Main-sequence K- and M-stars. *Astrophys. J.* **757**, 112 (2012).

37. Ricker, G. R. et al. Transiting Exoplanet Survey Satellite (TESS). *J. Astron. Telesc. Instrum. Syst.* **1**, 014003 (2015).

38. McMullin, J. P., Waters, B., Schiebel, D., Young, W. & Golap, K. CASA architecture and applications. In *Astronomical Data Analysis Software and Systems XVI, Astronomical Society of the Pacific Conference Series* Vol. 376 (eds Shaw, R. A. et al.) 127–130 (Astronomical Society of the Pacific, 2007).

39. Benz, A. O. & Guedel, M. X-ray/microwave ratio of flares and coronae. *Astron. Astrophys.* **285**, 621–630 (1994).

40. See, V. et al. Studying stellar spin-down with Zeeman–Doppler magnetograms. *Mon. Not. R. Astron. Soc.* **466**, 1542–1554 (2017).

41. Weber, E. J. & Davis, L. Jr. The angular momentum of the solar wind. *Astrophys. J.* **148**, 217–227 (1967).

42. Parker, E. N. Dynamics of the interplanetary gas and magnetic fields. *Astrophys. J.* **128**, 664 (1958).

43. Stelzer, B., Marino, A., Micela, G., López-Santiago, J. & Liefke, C. The UV and X-ray activity of the M dwarfs within 10 pc of the Sun. *Mon. Not. R. Astron. Soc.* **431**, 2063–2079 (2013).

44. Loyd, R. O. P. et al. The MUSCLES Treasury Survey. III. X-ray to infrared spectra of 11 M and K stars hosting planets. *Astrophys. J.* **824**, 102 (2016).

45. Klein, B. et al. The large-scale magnetic field of Proxima Centauri near activity maximum. *Mon. Not. R. Astron. Soc.* **500**, 1844–1850 (2021).

46. Moutou, C. et al. SPIRou input catalogue: activity, rotation and magnetic field of cool dwarfs. *Mon. Not. R. Astron. Soc.* **472**, 4563–4586 (2017).

47. Morin, J. et al. Large-scale magnetic topologies of late M dwarfs. *Mon. Not. R. Astron. Soc.* **407**, 2269–2286 (2010).

48. Reiners, A. et al. Magnetism, rotation, and nonthermal emission in cool stars. Average magnetic field measurements in 292 M dwarfs. *Astron. Astrophys.* **662**, A41 (2022).

49. Vidotto, A. A. et al. M-dwarf stellar winds: the effects of realistic magnetic geometry on rotational evolution and planets. *Mon. Not. R. Astron. Soc.* **438**, 1162–1175 (2014).

50. Altschuler, M. D. & Newkirk, G. Magnetic fields and the structure of the solar corona. I: Methods of calculating coronal fields. *Sol. Phys.* **9**, 131–149 (1969).

51. Wood, B. E., Linsky, J. L., Müller, H.-R. & Zank, G. P. Observational estimates for the mass-loss rates of α Centauri and Proxima Centauri using Hubble Space Telescope Lyα spectra. *Astrophys. J. Lett.* **547**, L49–L52 (2001).

52. Wood, B. E. et al. New observational constraints on the winds of M dwarf dtars. *Astrophys. J.* **915**, 37 (2021).

53. Vidotto, A. A. The evolution of the solar wind. *Living Rev. Solar Phys.* **18**, 3 (2021).

54. Queinnec, J. & Zarka, P. Flux, power, energy and polarization of Jovian S-bursts. *Planet. Space Sci.* **49**, 365–376 (2001).

55. Astropy Collaboration Astropy: a community Python package for astronomy. *Astron. Astrophys.* **558**, A33 (2013).

56. Astropy Collaboration The Astropy Project: building an open-science project and status of the v2.0 core package. *Astron. J.* **156**, 123 (2018).

57. Reid, I. N., Hawley, S. L. & Gizis, J. E. The Palomar/MSU Nearby-Star Spectroscopic Survey. I. The northern M Dwarfs—band strengths and kinematics. *Astron. J.* **110**, 1838 (1995).

58. Hawley, S. L., Gizis, J. E. & Reid, I. N. The Palomar/MSU Nearby Star Spectroscopic Survey.II. The southern M dwarfs and investigation of magnetic activity. *Astron. J.* **112**, 2799 (1996).

59. Wargelin, B. J., Saar, S. H., Pojmański, G., Drake, J. J. & Kashyap, V. L. Optical, UV, and X-ray evidence for a 7-yr stellar cycle in Proxima Centauri. *Mon. Not. R. Astron. Soc.* **464**, 3281–3296 (2017).

60. Reiners, A. et al. The CARMENES search for exoplanets around M dwarfs. High-resolution optical and near-infrared spectroscopy of 324 survey stars. *Astron. Astrophys.* **612**, A49 (2018).

61. Newton, E. R., Mondrik, N., Irwin, J., Winters, J. G. & Charbonneau, D. New rotation period measurements for M dwarfs in the Southern Hemisphere: an abundance of slowly rotating, fully convective stars. *Astron. J.* **156**, 217 (2018).

62. Irwin, J. et al. On the angular momentum evolution of fully convective stars: rotation periods for field M-dwarfs from the MEarth Transit Survey. *Astrophys. J.* **727**, 56 (2011).

63. Reiners, A. & Basri, G. The moderate magnetic field of the flare star Proxima Centauri. *Astron. Astrophys.* **489**, L45–L48 (2008).

64. Faria, J. P. et al. A candidate short-period sub-Earth orbiting Proxima Centauri. *Astron. Astrophys.* **658**, A115 (2022).

65. Anglada-Escudé, G. et al. A terrestrial planet candidate in a temperate orbit around Proxima Centauri. *Nature* **536**, 437–440 (2016).

Acknowledgements

Author contributions

J.S.P. identified the target, developed models of the stellar environment, and the calculated star–planet interaction flux density predictions. J.V. developed the observing strategy, and reduced and analysed the radio data. Both authors contributed heavily to interpreting results and writing the paper.

Competing interests

The authors declare no competing interests.

Additional information

Supplementary information The online version contains supplementary material available at https://doi.org/10.1038/s41550-023-01914-0.

Correspondence and requests for materials should be addressed to J. Sebastian Pineda.

Peer review information *Nature Astronomy* thanks Rachel Osten and the other, anonymous, reviewer(s) for their contribution to the peer review of this work.

Reprints and permissions information is available at www.nature.com/reprints.

Publisher's note Springer Nature remains neutral with regard to jurisdictional claims in published maps and institutional affiliations.